



MOF-biochar nanocomposite for sustainable remediation of contaminated soil

Vladimir Polyakov¹ · Tatiana Bauer¹ · Mikhail Kirichkov¹ · Vera Butova^{1,2} · Maksim Gritsai¹ · Tatiana Minkina¹ · Alexander Soldatov¹ · Ekaterina Kravchenko¹

Received: 11 November 2024 / Accepted: 30 January 2025
© The Author(s), under exclusive licence to Springer-Verlag GmbH Germany, part of Springer Nature 2025

Abstract

Soil contamination by heavy metals represents a critical environmental risk. Innovative and sustainable remediation strategies are urgently needed to address this global challenge. Biochar, derived from biomass pyrolysis, has gained attention as an eco-friendly material for heavy metal adsorption. However, its adsorption performance is highly dependent on the pyrolysis conditions and can be further enhanced through functionalization. In this study, wheat straw biochar was optimized for enhanced porosity, carbon content, and structural stability and further functionalized by incorporating metal–organic frameworks (MOFs) to create a high-performance nanocomposite. Three MOFs—ZIF-8, UiO-66, and MIL-100(Fe)—were evaluated for their Cu²⁺ and Pb²⁺ adsorption capacities. MIL-100(Fe) emerged as the most effective due to its high pore volume and iron-active sites. Coating biochar with MIL-100(Fe) increased its surface area sixfold, achieving 419 m²·g⁻¹, and doubled its sorption capacity for heavy metals in soil (142 mmol·kg⁻¹ for Cu²⁺ and 156 mmol·kg⁻¹ for Pb²⁺). Advanced characterization techniques, including XAFS, XRD, and SEM–EDX, revealed that the sorption mechanisms were dominated by complexation and cation exchange, with the nanocomposite demonstrating superior metal immobilization compared to neat biochar. These findings highlight the potential of the nanocomposite as an effective amendment for reducing heavy metal toxicity in soils.

Keywords Metal–organic framework · Biochars · Nanocomposite · Heavy metals · Adsorption

Introduction

Soil contamination by heavy metals (HMs) has become a global concern, largely due to ongoing urbanization and industrialization (Wuana and Okieimen 2011). Various industrial activities, along with the rapid expansion of urban areas, have significantly contributed to soil pollution (Thakur et al. 2022). A study on the spatiotemporal variability of cadmium in the soils of Guangxi, China, identified non-ferrous metallurgy and related non-ferrous metal mining as key contributors to HM enrichment in the region (Tian

et al. 2023). Using a positive matrix factorization model, researchers Chandra et al. (2023) estimated the cancer risks of HMs entering the soil through agricultural activities and transport emissions. While fertilizers are crucial for enhancing crop productivity, their excessive use has altered the soil chemistry, leading to increased HM levels in the soil (Kravchenko et al. 2025). These metals, particularly copper (Cu) and lead (Pb), pose serious risks to plants, animals, and human health. Copper accumulation in soil impairs water and nutrient uptake, disrupts photosynthesis, and stunts plant growth (Rodrigues Cruz et al. 2022). Lead toxicity arises from its ability to inhibit porphobilinogen synthase, a key enzyme in heme biosynthesis, leading to anemia (Abadin et al. 2007). Consequently, developing effective methods for soil remediation is a critical challenge for researchers worldwide.

Carbon-based sorbents like biochar, activated carbon, graphene, graphene oxide, carbon nanotubes, and soot are effective for the remediation of HM-contaminated soil (Fu et al. 2022). Biochar, a solid carbon-rich material produced

Responsible Editor: Kitae Baek

✉ Ekaterina Kravchenko
ekakra@sfedu.ru

¹ Southern Federal University, 344090 Rostov-On-Don, Russia

² Institute of General and Inorganic Chemistry, Bulgarian Academy of Sciences, Sofia 1113, Bulgaria

via biomass pyrolysis, stands out due to its structural properties. Its high surface area enhances interaction with contaminants, while its porous nature physically traps ions. Biochar's surface functional groups, both negatively and positively charged, attract and retain ions such as ammonium (NH_4^+), metal ions, phosphate (PO_4^{3-}), and nitrate (NO_3^-) (Vasseghian et al. 2024). Additionally, these groups form complexes with the adsorbed species, further boosting the adsorption capacity. These properties make biochar a highly effective adsorbent for the removal of HMs in soils. It has recently been widely used as a potential soil additive to improve its properties. It has been proven that biochar improves soil structure by reducing bulk density, increasing porosity, and enhancing water retention, particularly under drought conditions (Kravchenko et al. 2023). It also enhances nutrient availability, supports microbial activity, and raises soil pH, leading to better plant growth and higher yields (Wu et al. 2023).

Biochar also reduces the bioavailability and mobility of HMs in contaminated soils, decreasing their uptake by plants (Anbalagan et al. 2023). Feedstock choice significantly influences biochar's properties. Burachevskaya et al. (2023) studied biochars derived from wood, sunflower husks, and rice husks and noted that their adsorption capacities vary, with wood biochar demonstrating the highest efficiency due to its specific surface area and aromatic functional groups. Optimized pyrolysis conditions, such as those applied to rice husk biochar, further enhance its potential as a sorbent (Lobzenko et al. 2022). However, biochar has its limitations. When produced under suboptimal conditions, it may have low sorption capacities, reducing its effectiveness in environmental applications like soil remediation. Enhancing the sorption properties of biochar remains a critical scientific challenge, necessitating further optimization of pyrolysis parameters and careful selection of feedstocks to fully realize its potential in practical use.

Composite biochar materials show promise in overcoming biochar limitations. Gouma et al. (2022) found that magnetic biochar allows for easy retrieval from soil, allowing for the removal of both contaminants and the sorbent. Similarly, combining biochar with metal-tolerant bacteria has enhanced its performance in decontaminating zinc-contaminated soil, reducing zinc uptake by plants while improving their growth and health (Rajput et al. 2023). Gholizadeh and Hu (2021) provided a detailed analysis of various materials based on biochar doped with metals, metal oxides or sulfides, and non-metals (sulfur and phosphorus), as well as various fertilizers (hydroxyapatite, calcium silicate, struvite, clay) and organic substances (chitosan). In addition, various mechanisms of HM binding by composites were considered. Mazarji et al. (2023) conducted a similar comparative study and showed that one of the most successful combinations is the combination of biochar with Fe_3O_4 , FeS nanoparticles,

graphene oxide, or chitosan. These advancements highlight biochar's adaptability and potential for sustainable soil remediation.

One of the most promising modern approaches is combining biochar with metal-organic frameworks (MOFs) (Butova et al. 2016b). MOFs are porous materials consisting of metallic ions or clusters connected by organic molecules, forming stable, highly customizable structures with exceptional porosity (Tranchemontagne et al. 2009). Their modular design enables precise tuning of the pore size, functionality, and catalytic properties. These characteristics give the MOFs superior performance in HM adsorption. For instance, MIL-100(Fe) has demonstrated high sorption capacity for As^{5+} removal from aqueous systems, while Cu-BTC has effectively removed Hg^{2+} (Khan et al. 2013). Peng et al. (2018) developed a versatile HM ion trap using MOF-808 modified with ethylenediaminetetraacetic acid (EDTA), capable of removing 22 different metal ions. Rani et al. (2020) compared the efficiency of various MOFs in removing $\text{As}^{5+}/\text{As}^{3+}$, Cr^{3+} , Cd^{2+} , Hg^{2+} , and Pb^{2+} .

With exceptionally high surface areas, MOFs enable strong interactions with heavy metal ions, thereby enhancing adsorption. For example, UiO-66 derivatives, with their high porosity and Lewis acid-base interactions, achieved adsorption capacities of $232 \text{ mg}\cdot\text{g}^{-1}$ for Pb^{2+} , $303 \text{ mg}\cdot\text{g}^{-1}$ for $\text{As}(\text{V})$, and $769 \text{ mg}\cdot\text{g}^{-1}$ for $\text{Hg}(\text{II})$. MIL-100(Fe) provides unsaturated metal centers essential for adsorption, showing composite capacities of $286 \text{ mg}\cdot\text{g}^{-1}$ for $\text{Cr}(\text{VI})$ and $143\text{--}115 \text{ mg}\cdot\text{g}^{-1}$ for $\text{As}(\text{III})$. ZIF-8, known for its high porosity and surface area, exhibited a remarkable sorption capacity of $1120 \text{ mg}\cdot\text{g}^{-1}$ for Pb^{2+} , facilitated by hydrogen bonding, acid-base interactions, and surface hydroxyl groups.

Combining MOFs with other materials often results in synergistic performance improvements. Bui et al. (2025) found that a composite of UiO-66, BiVO_4 , and Mo_2CT_x significantly enhanced photocatalytic atrazine degradation by leveraging light absorption and excellent conductivity. Similarly, a combination of UiO-66- NH_2 , polyvinyl alcohol, and graphene oxide showed superior adsorption of pollutants like perfluorooctanoic acid compared to any individual component (Van Thang et al. 2024). This synergy arises from multiple mechanisms such as electrostatic and hydrophobic interactions, working together to improve contaminant capture.

While MOFs exhibit remarkable potential for HM adsorption, their structure and properties are highly influenced by the synthesis and post-synthetic treatment methods used. Even the same type of MOF can display significant variations in properties across different studies, depending on the protocols applied. Additionally, the scalability of MOF synthesis can be challenging for certain structures due to complex multi-step processes or the need for custom-made linkers.

Given the extensive range of MOF structures, three well-studied and representative MOFs—ZIF-8, UiO-66, and MIL-100(Fe)—were selected for this study. These MOFs were chosen for their reproducible synthesis protocols, commercial availability, and established scalability as demonstrated in prior works: UiO-66 (Ragon et al. 2014), ZIF-8 (Quan et al. 2023), and MIL-100 (Ahmed et al. 2023). A comparative analysis of these MOFs allowed the evaluation of key factors such as pore size and shape, active site accessibility, stability, and porosity in relation to their HM adsorption performance.

UiO-66 is constructed from $Zr_6O_4(OH)_4$ clusters connected by 1,4-benzenedicarboxylate (terephthalate) linkers, resulting in a porous 3D framework with tetrahedral pores of approximately 8 Å and octahedral pores of about 11 Å (Cavka et al. 2008). ZIF-8, on the other hand, is built from zinc-nitrogen tetrahedra (ZnN_4), where the nitrogen atoms are part of the imidazole ring of the 2-methylimidazolate linker. This gives ZIF-8 a sodalite topology with spherical pores roughly 11 Å in diameter (Park et al. 2006). MIL-100(Fe) consists of iron (III) octahedral trimers linked by trimesic acid, creating a framework with mesoporous cages. These cages feature apertures of approximately 25 and 29 Å, which are accessible through microporous windows of approximately 5.5 and 8.6 Å (Horcajada et al. 2007).

The goal of this research was to develop an effective composite for the adsorption of Cu^{2+} and Pb^{2+} ions. Wheat straw biochar is selected as the base material for the composite, and pyrolysis conditions are optimized to maximize yield and porosity. To enhance the composite's sorption performance, the introduction of one of three MOFs—UiO-66, MIL-100, or ZIF-8—was considered. The optimal MOF was selected based on its stability and HM adsorption capacity. These two optimized components are then combined to create a composite for remediating soil contaminated with Cu^{2+} and Pb^{2+} ions.

Materials and methods

Materials

Zirconium(IV) chloride anhydrous, iron powder, zinc nitrate hexahydrate, lead(II) nitrate, copper(II) nitrate trihydrate, hydrofluoric acid, nitric acid, 1,4-benzenedicarboxylic (terephthalic) acid, 1,3,5-benzenetricarboxylic (trimesic) acid, 2-methylimidazole, dimethylformamide (DMF), and isopropanol were purchased from Sigma-Aldrich Co. (St. Louis, MO, USA). Deionized water (18 M Ω -cm) was obtained from the Simplicity UV water purification system.

Synthesis

Optimization of wheat straw biochar properties

Wheat straw (WS) was used as feedstock. Before pyrolysis, the straw was washed with deionized water and subsequently dried at room temperature. The samples were then successively heated at 105 °C in an oven to ensure complete moisture removal. Dried and partially chopped straw was loaded into a laboratory pyrolysis unit and placed in a muffle oven, passing a flow of nitrogen at a flow rate of 50 ml/min to create an inert atmosphere. The standard pyrolysis conditions were applied, which included a pyrolysis temperature of 500 °C, a heating rate of 10 °C•min⁻¹, and a retention time of 60 min (Abbas et al. 2018). To optimize these conditions, a systematic approach was employed by varying one parameter at a time: temperature ranging from 300 to 900 °C, retention time from 10 to 75 min, and heating rate from 5 to 30 °C•min⁻¹. Throughout these optimizations, two other parameters were kept constant in accordance with the standard procedure (Table S1).

UiO-66 synthesis

The synthesis followed a previously described procedure (Butova et al. 2019). Initially, 504.2 mg (2.16 mmol) of zirconium (IV) chloride $ZrCl_4$ was dissolved by stirring in 50 ml of DMF. Subsequently, 116.7 μ l of deionized water was added to the solution. Then, 359.1 mg (2.16 mmol) of terephthalic acid was added. The resulting mixture was stirred using a magnetic stirrer until complete dissolution. The resulting solution was transferred to a glass flask and placed in a muffle furnace preheated to 120°C for 24 h. Afterward, the flask was then allowed to cool to room temperature, and the resulting white precipitate was washed twice with DMF and twice with isopropanol via centrifugation. Finally, the powder was dried in an oven at 60°C.

ZIF-8 synthesis

ZIF-8 was synthesized using a method previously developed by Butova et al. (2016a). Initially, 0.2658 g (0.669 mmol) of zinc nitrate hexahydrate $Zn(NO_3)_2 \cdot 6H_2O$ was dissolved in 10 ml of DMF. Separately, 0.2194 g (2.676 mmol) of 2-methylimidazole was dissolved in another 10 ml of DMF. Both solutions were combined and transferred into a Teflon ampoule, which was then inserted in a CEM Mars6 microwave oven. The resulting solution was heated to 140 °C for 15 min under magnetic stirring and a microwave irradiation power of 600 W. Once the reaction was complete, the ampoule was cooled to room temperature, and the resulting

white precipitate was washed twice with DMF and once with isopropanol via centrifugation. Subsequently, the sample was dried at 60 °C.

MIL-100(Fe) synthesis

According to the synthesis technique (Gorban et al. 2020), 0.33 g (5.893 mmol) of iron powder and 0.84 g (4 mmol) of trimesic acid were added to 30 ml of deionized water. This mixture was stirred for 30 min, after which concentrated hydrofluoric acid HF (0.2 ml) and concentrated nitric acid HNO₃ (0.15 ml) were added. The resulting mixture in a Teflon ampoule was then placed in a steel autoclave and heated at 120°C for 20 h. After cooling, the resultant orange precipitate underwent three washes with deionized water before being dried at 60°C. The sample is referred to as MIL-100 in the following text.

Sorption experiments

Solutions of Cu(NO₃)₂ and Pb(NO₃)₂ were prepared at concentrations of 0.005, 0.02, 0.06, and 0.1 M. MOFs were activated at 150 °C for 2 h in a vacuum oven. Subsequently, 25 mg of the respective MOF powder was added to 25 ml of the respective HM solution. The suspensions were stirred for 4 h. Subsequently, MOFs were washed once with ice-cold water, separated by centrifugation, and dried at 60°C.

WSB@MIL-100 nanocomposite synthesis

A total of 0.33 g (5.893 mmol) of iron powder, 0.84 g (4 mmol) of trimesic acid, and 2.3 g of biochar were added to 30 ml of deionized water. After the formation of the black suspension, stirring was continued for 30 min. Subsequently, 0.2 ml of concentrated hydrofluoric acid (HF) and 0.15 ml of concentrated nitric acid (HNO₃) were introduced. The resulting mixture was transferred to a Teflon ampoule, which was then placed in a steel autoclave and heated at 120°C for 20 h. Upon cooling, the resultant black precipitate underwent three washes with deionized water, was separated via centrifugation, and dried at 60°C.

Characterization

Biochar characterization

The yield of biochar was determined by calculating the mass ratio of biochar to feedstock as per the following equation:

$$\text{Yield} = \frac{W_{\text{biochar}}}{W_{\text{biomass}}} \cdot 100\% \quad (1)$$

where W_{biochar} and W_{biomass} are biochar and biomass weight in kilogram.

The potentiometric method was employed to measure the pH values of both plant materials and their respective biochars. This involved mixing 1 g of sample with 20 ml of deionized water, shaking the mixture on a shaker for 10 min, and allowing it to settle for 5 min before conducting pH measurements (Bordoloi et al. 2015). The ash content was estimated from the residual mass after burning the biochar samples in a muffle furnace at 750°C for 6 h. The element compositions (C, H, N) of the biochars were analyzed using the PE 2400 Series II CHN Analyzer (Perkin Elmer, USA). Oxygen (O) was determined by the difference in mass, considering that the whole biomass is composed of C, H, N, O, and ash.

The results of the elemental composition study were used to calculate the atomic H/C and O/C ratios, characterizing the degree of aromaticity and carbonization of the obtained materials (Tu et al. 2020).

The specific surface area (SSA) was determined using the Brunauer–Emmett–Teller (BET) model. These isotherms were measured using a Micromeritics ASAP 2020 instrument (Micromeritics, USA). Prior to measurements, samples underwent activation at 150 °C for 10 h under dynamic vacuum conditions. The total pore volume was determined from the adsorption branches of the isotherms at a point near a relative pressure P/P_0 of 0.97.

Characterization of the MOFs and WSB@MIL-100 composite

The phase composition of the synthesized MOFs and the WSB@MIL-100 composite sample was analyzed using a Bruker D2 Phaser X-ray diffractometer (XRD) equipped with a Lynxeye detector, operating with Cu-K α radiation (1.541874 Å). Diffraction patterns were recorded over a range of 5° to 90°, with a step size of 0.01°. X-ray diffraction pattern analysis was conducted using the COD2016 database (version COD-inorg 2022.06.29) and the ICSD (Inorganic Crystal Structure Database). Phase identification was performed with the software package Match! Version 3.15 (Crystal Impact GbR, Bonn, Germany).

Fourier transform infrared (FTIR) spectra were obtained using a Vertex 70 spectrometer (Bruker, Germany) with ATR (attenuated total reflectance) geometry, utilizing an MCT detector and a Bruker Platinum ATR accessory. Spectra were recorded between 5000 and 500 cm⁻¹ at a resolution of 1 cm⁻¹ with 64 scans. A reference spectrum was recorded under atmospheric conditions.

Transmission electron microscopy (TEM) images were taken with a Tecnai G2 Spirit BioTWIN microscope (FEI, Netherlands) to examine the morphology and size of the synthesized crystallites. Additionally, SEM–EDS elemental distribution maps of the biochar and composite were captured using a Helios Nanolab 660 microscope (Center for

Collective Usage “Systems for Microscopy and Analysis,” Skolkovo, Moscow, Russia). The elemental composition was further assessed through micro-X-ray fluorescence (XRF) using an M4 TORNADO spectrometer (Bruker, Billerica, MA, USA).

Sorption of HMs in soil amended with biochar and the WSB@MIL-100 nanocomposite

The soil used in this research was gathered from the top-soil layer (0–20 cm) of a Haplic Chernozem (Clayic) soil type sourced from an undisturbed protected natural area located in the Rostov region (Russia). The soil had a pH of 7.3 (water/soil = 2.5:1.0, v/w), C_{org} of 3.6%, CaCO_3 of 0.5%, cationic exchange capacity of $41.1 \text{ cmol}^+ \cdot \text{kg}^{-1}$; exchangeable cations ($\text{cmol}^+ \cdot \text{kg}^{-1}$): Ca^{2+} of 33.4, Mg^{2+} of 4.6; silt particles (< 0.01 mm) of 52.1% and clay particles (> 0.001 mm) of 25.2%. The fresh soil samples were air-dried, and the plant roots were removed and passed through a 2-mm sieve before use.

The biochar and nanocomposite were integrated into the soils by mixing the soil with the measured amounts of sorbents on a rotary shaker for 5 days. The sorbent ratio (w/w) in the amended soils was set to 2% (intermediate application rate). Metal sorption was investigated through batch experiments on both sorbent-free soil and sorbent-amended soils to comprehensively examine the impact of biochar and nanocomposite amendments on HM sorption in soil.

The sorption experiments were conducted in 150-ml Erlenmeyer flasks at a temperature of 25 °C. Cu^{2+} and Pb^{2+} solutions were prepared by dissolving their respective nitrate salts in deionized water. The initial HM concentrations in the solutions were 0.5, 1, 2, 4, 6, 8, and 10 mM. Although 10 mM is a relatively high concentration of heavy metals in soils, industrialized regions often exhibit extreme levels of Pb and Cu contamination (Hou et al. 2023; Nunn et al. 2025). We used single HM solutions rather than combinations because previous studies have shown that in contaminated soils, despite the presence of multiple metals, one dominant metal often far exceeds threshold levels, sometimes by several orders of magnitude compared to others (Linnik et al. 2022; Minkina et al. 2018). The concentration of this dominant pollutant is the primary factor influencing the ecological condition of soils.

Five grams of either soil, biochar-amended soil, or nanocomposite-amended soil was combined with 50 ml of HM solution in the flasks. The initial pH of the solutions was adjusted by adding dilute solutions of 0.1 M KOH and HNO_3 . The flasks were sealed with silicon caps and agitated at 200 rpm on a rotary shaker for 1 h, followed by 24 h of quiescent settling to achieve apparent equilibrium, as previous investigations have indicated that equilibrium was attained within this time frame (Burachevskaya et al. 2023). Subsequently,

the solutions were filtered, and the concentrations of Cu^{2+} and Pb^{2+} in the supernatant were determined using an atomic absorption spectrophotometer (AAS, MGA-915 AA, Lyumeks, Russia).

Data analysis

The adsorption capacity, denoted as C_{ad} ($\text{mmol} \cdot \text{kg}^{-1}$), was determined using the following equation:

$$C_{\text{ad}} = \frac{(C_i - C_{\text{eq}}) \times V}{m} \quad (2)$$

where C_i and C_{eq} (in mM) represent the initial and equilibrium solution metal concentrations, respectively. V (in ml) denotes the volume of the solution, while m (in g) represents the mass of the sorbent. This data was utilized to generate the $C_{\text{eq}}-C_{\text{ad}}$ plot.

The removal efficiency was calculated by determining the percentage sorption using the following equation:

$$\text{Removal} = \frac{C_i - C_{\text{eq}}}{C_i} \cdot 100\% \quad (3)$$

The adsorption isotherms were modeled using the Langmuir and Freundlich equations:

$$C_{\text{ad}} = C_m \frac{K_L C_{\text{eq}}}{(1 + K_L C_{\text{eq}})} \quad (4)$$

where C_m ($\text{mmol} \cdot \text{kg}^{-1}$) represents the maximum adsorption capacity for the metal, while C_{eq} (in mM) denotes the concentration of metal at equilibrium. K_L (in $\text{L} \cdot \text{mmol}^{-1}$) is the Langmuir model constant, reflecting the affinity of the binding sites (Cui et al. 2016).

$$C_{\text{ad}} = K_F C_{\text{eq}}^{1/n} \quad (5)$$

where K_F ($\text{L} \cdot \text{kg}^{-1}$) stands for the Freundlich adsorption constant, and $1/n$ represents the Freundlich exponent related to adsorption intensity (Cui et al. 2016).

Sorption isotherm experiments were performed in triplicate, and the standard deviation was calculated using descriptive statistics with the STATISTICA software package. The sorption isotherms were then fitted using the Origin Pro 8.0 software package, and the correlation coefficient (R^2) values were used to assess and compare the performances of the Langmuir and Freundlich models.

Mechanisms of HM sorption by biochar- and nanocomposite-amended soils

To discern the mechanisms of interaction between HM and both the sorbents and the mineral and organic phases of soil,

we conducted XRD analysis on three sample groups: soil samples without sorbent additives, soil samples with WSB additives, and soil samples with nanocomposite additives. For reference, we also included soil samples without any sorbent additives and those not uncontaminated with metal nitrates. The mineral phase concentrations were calculated using the Reference Intensity Ratio method (Madsen et al. 2019). The relative intensity of the X-ray diffraction patterns was automatically set such that the intensity of the most prominent diffraction peak was equal to 1000 conventional units.

X-ray absorption spectroscopy (XAS) measurements were conducted at the National Research Center Kurchatov Institute using the experimental station “Structural Materials Science” STM (K1.3b). The local atomic structure of the soil samples with sorbents was measured in the region of the K-edges of Cu (8979 eV) and the L_{III} -edge of Pb (13,035 eV). The analysis included both X-ray absorption near edge structure (XANES) and extended X-ray absorption fine structure (EXAFS). The near-edge region of the XANES spectra is particularly sensitive to bond geometry. The method was applied for a preliminary qualitative analysis of the environment of metals in samples of contaminated soil without adding sorbents and soil and with the addition of biochar and nanocomposite. Compounds of metal nitrates in which the nearest coordination spheres of metal atoms are formed by oxygen and nitrogen atoms ($Me(NO_3)_2$) were used as reference samples. The experimental spectra were normalized, after which the oscillating part of the EXAFS function $\chi(k)$ was separated from the absorption spectra by the Fourier transform.

SEM–EDX analysis of soils was carried out at ITMO University Core Facility Center “Nanotechnologies” (St. Petersburg, Russia) using FEI Quanta Inspect with the EDX attachment microscope at an accelerating voltage of 20 kV. Elemental mapping and element identification were carried out in a semi-automatic mode using the energy-dispersive X-ray spectroscopy database.

Results and discussion

Optimization of biochar synthesis

The physicochemical properties of the biochars obtained under various pyrolysis conditions are summarized in Table S1. Optimizing these conditions is crucial because they significantly influence product yield distribution. A notable observation is that increasing the pyrolysis temperature reduced the biochar yield from 53.47 to 24.7% (Table S1). The most substantial mass loss occurred between 300 and 700°C, primarily due to dehydration and the release of volatile substances and non-condensable gases (Brassard

et al. 2019). Above 700°C, the reduction in biochar yield slowed because this range was associated with the complete thermal decomposition of hemicellulose, cellulose, and lignin. In contrast, the effects of pyrolysis time and heating rate were less pronounced: increasing the retention time from 10 to 75 min and the heating rate from 5 to 30°C/min resulted in weight losses of only 4.82% and 3.37%, respectively.

The initial pH of wheat straw was neutral (pH 7.14). However, as the temperature, retention time, and heating rate of pyrolysis increased, the pH values of the resulting biochars also increased from 9.27 to 10.42 (Table S1). Among the parameters considered, temperature played a pivotal role in the alteration of the pH values of the obtained samples. This phenomenon is attributed to the destruction and loss of acidic functional groups (such as phenolic and carboxylic groups) as the temperature increases (Kaur et al. 2023).

According to the analysis results of the feedstock elemental composition, it has been shown that the ash content of wheat straw is 5.43%, carbon content 46.34%, oxygen 42.36%, hydrogen 5.16, and nitrogen 0.71% (Table S1). The ash and C contents of the biochar increased with pyrolysis temperature and time, whereas the H, N, and O contents declined.

The increase in the carbon (C) content of biochar with increasing pyrolysis temperature can be explained by the higher rate of carbonization and the development of aromatic carbon structures (Zhang et al. 2020). The increase in the C content with the extended pyrolysis time was due to the accelerated loss of long-chain aliphatic groups through the homolytic dissociation of C–C and C–H bonds. The result of prolonged thermal exposure exceeds the energy threshold for bond dissociation, leading to the formation of more stable structures (Cimò et al. 2014). The decrease in hydrogen (H) and oxygen (O) content with increasing pyrolysis parameters is likely due to the loss of water vapor and volatile substances (CO_2 , H_2 , and CO) as lignocellulose decomposes. The nitrogen (N) content in biochar generally depends more on the feedstock type than on the pyrolysis conditions (Zhao et al. 2018). The slight reduction in nitrogen at higher temperatures can be attributed to the loss of volatile nitrogenous compounds, such as NH_4^+ and NO_3^- , as well as the NH_2 groups of organic compounds (Khanmohammadi et al. 2015).

The effect of heating rate on the elemental composition of biochar differed from that of temperature and time parameters. As the heating rate increased from 5 to 15 °C•min⁻¹, the C and ash contents increased, and the O, H, and N contents decreased. At higher heating rates (20 and 30 °C•min⁻¹), the opposite trends were observed. Similar effects of heating rates (5, 10, 20, and 30 °C•min⁻¹) on the elemental composition of pyrolysis products from Moso bamboo were reported

by Chen et al. (2014). It was found that as the heating rate increased, ash and oxygen contents increased, while carbon content in the biochar decreased. The quality of the resulting biochar can be assessed by calculating the atomic ratios of H/C and O/C, showing the product's degree of aromaticity, carbonization, and oxidation stability (Leng et al. 2019). Changes in the H/C and O/C ratios of biochar can be used to indicate possible chemical reaction pathways during biochar production.

Analysis of the obtained data showed that as the pyrolysis temperature increased, the atomic ratios of H/C and O/C decreased from 0.74 to 0.26 and from 0.28 to 0.03, respectively. The progressive decrease in the H/C and O/C ratios with increasing pyrolysis temperature indicates a trajectory associated with the dehydrogenation and deoxygenation reactions of cellulose and lignin (Zhou et al. 2021). Pyrolysis time has a similar but less pronounced effect: as the time increases from 10 to 75 min, the atomic ratios of H/C and O/C decrease from 0.63 to 0.27 and from 0.18 to 0.03. Increasing the heating rate led to different effects. As the heating rate increased from 5 to 15 °C•min⁻¹, the H/C and O/C ratios are 0.43–0.28 and 0.05–0.04, respectively. A further increase in the heating rate increased in the H/C and O/C ratios.

According to The International Biochar Initiative (2022) and the European Biochar Certificate (2012–2022), the minimum H/C and O/C ratios for carbonized products should be 0.7 and 0.4, respectively, to distinguish them from unmodified or slightly charred biomass (Zhang et al. 2020). All samples were obtained at a temperature of 300–900 °C, 10–75 min, and a heating rate of 5–30 °C•min⁻¹ met these requirements (Table S1).

The prediction of the half-life of biochar made by Spokas (2010) suggests that an O/C ratio < 0.2 produces a stable carbonized material whose half-life can be > 1000 years. According to the results obtained, almost all samples fall into this category. The exception is the sample obtained at 300 °C. This suggests that the pyrolysis temperature of wheat straw primarily influences the stability of biochar.

Pyrolysis induces significant transformations in the raw feedstock, resulting in biochar as the final product. Beyond this stage, additional heating does not cause major structural changes. However, extended pyrolysis can degrade the functional groups on the biochar's surface, hindering subsequent MOF grafting for composite production. Therefore, the optimal pyrolysis conditions lie in the range where the feedstock has been fully converted to biochar while retaining the surface functional groups essential for further modification. In this study, biochar production was optimized based on several characteristics, including yield, pH, ash content, and elemental composition. As a result, we determined that the optimal pyrolysis conditions were a temperature of 700°C, retention time of 45 min, and heating

rate of 10°C•min⁻¹. Under these conditions, the resulting material is fully converted to biochar, free of transient components such as water and volatile organics, yet retains the functional groups critical for composite production. The resulting biochar, designated as WSB, had an SSA of 72 m²•g⁻¹ and a total pore volume of 0.046 cm³•g⁻¹ (Fig. S1 in supplementary materials).

MOF basic characterization

The three synthesized MOFs were thoroughly characterized. Powder XRD profiles (Fig. S2 in supplementary materials) confirmed that all MOFs are single-phase, highly crystalline compounds. UiO-66 was identified with an Fm-3m face-centered cubic structure (Cavka et al. 2008), ZIF-8 with cubic symmetry and the I-43m space group (Butova et al. 2017), and MIL-100 with the Fd-3m space group (Horcajada et al. 2007), consistent with previously reported data. FTIR spectroscopy (Fig.S3 in supplementary materials) further validated the purity of the MOFs. TEM images (Fig. 1a, Fig.S4a in supplementary materials) revealed that UiO-66 consists of octahedral nanoparticles around 150 nm in size. ZIF-8 showed a narrower particle size distribution, ranging from 40 to 100 nm, with an average size of 55 nm (Fig. 1b, Fig.S4b in supplementary materials). In contrast, MIL-100 formed larger particles ranging from 0.1 to 3 μm (Fig. 1c, Fig.S4c in supplementary materials).

The N₂ adsorption–desorption isotherms of the samples are shown in Fig. 1d. According to the IUPAC classification, the isotherms confirmed the microporous nature of all three materials. The MIL-100 isotherm exhibits two distinct

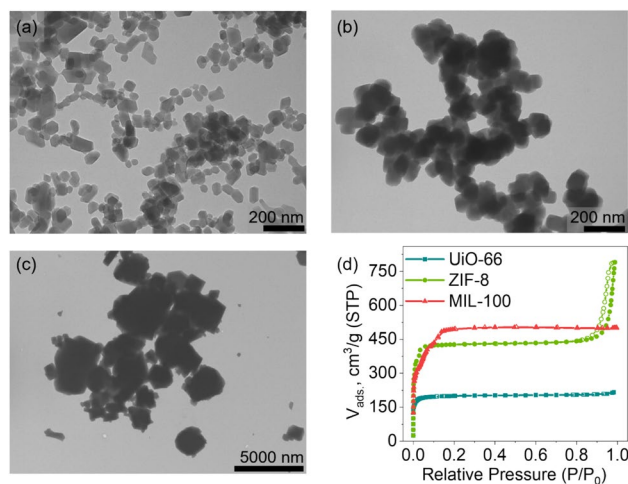


Fig. 1 Representative TEM images of the synthesized ZIF-8 (a), UiO-66 (b), and MIL-100 (c) samples. Part (d) shows the N₂ adsorption/desorption isotherms for the synthesized MOFs: UiO-66 (square markers), ZIF-8 (circle markers), and MIL-100 (triangle markers). Filled markers represent the adsorption branches of the isotherms, while empty markers indicate the desorption branches

microporous windows and mesoporous cages, resulting in two notable uptake points (Horcajada et al. 2007). ZIF-8 shows a pronounced hysteresis loop, which is attributed to capillary condensation of N_2 molecules in the uniform-sized particle spaces, as indicated by the narrow particle size distribution. A smaller hysteresis loop was observed for UiO-66, whereas no such loop was observed for MIL-100, likely due to the broader particle size distribution.

All three MOFs demonstrated high SSA: UiO-66 with $806 \text{ m}^2 \cdot \text{g}^{-1}$ (pore volume $0.33 \text{ cm}^3 \cdot \text{g}^{-1}$), ZIF-8 with $1739 \text{ m}^2 \cdot \text{g}^{-1}$ (pore volume $0.96 \text{ cm}^3 \cdot \text{g}^{-1}$), and MIL-100 with $1807 \text{ m}^2 \cdot \text{g}^{-1}$ (pore volume $0.77 \text{ cm}^3 \cdot \text{g}^{-1}$) (Fig. S5, Table S2 in supplementary materials).

HM adsorption by MOFs

After completing the basic characterization of the MOFs, we evaluated their specific HM adsorption performance. A key factor to consider is the stability of the sorbent in the solution. The stability of the MOF samples was assessed by analyzing their structure after exposure to the most concentrated (0.1 M) solutions of Cu^{2+} and Pb^{2+} salts. The XRD powder patterns before and after the sorption experiment are shown in Fig. 2.

The ZIF-8 phase was destroyed upon interaction with both HM salts. This breakdown can be attributed to the acidic environment produced by the hydrolysis of Cu^{2+} and Pb^{2+} ions. The dynamics of changes in the pH of Cu^{2+} and Pb^{2+} nitrate solutions before and after sorption are shown in Figure S6 (in supplementary materials). At $\text{pH} \leq 6$, 2-methylimidazole detaches from the ZIF-8 framework, leading to its complete decomposition (Avci et al. 2015). After Cu^{2+} adsorption, the XRD pattern revealed the formation of the $\text{Cu}_4(\text{NO}_3)_2(\text{OH})_6$ phase (Nowacki and Scheidegger 1952), while Pb^{2+} adsorption led to the appearance of $\text{Pb}(\text{NO}_3)_2$ (Nowotny and Heger 1986) and $\text{Pb}_3(\text{OH})_2(\text{CO}_3)_2$ (Siidra et al. 2018) (Fig. S7 in supplementary materials). This

indicates that the ZIF-8 framework reacted with Cu^{2+} and Pb^{2+} ions, resulting in the formation of precipitates.

While this reaction could be considered an alternative decontamination mechanism, it was not optimal for creating a stable composite with biochar, as our goal was to develop a durable sorbent for multiple uses. Therefore, we focused on the sorption capacities of the two other MOFs, which demonstrated high stability under acidic conditions.

Figure 3 shows the correlation between the sorption capacity (SC) of the UiO-66 and MIL-100 samples and the concentrations of the corresponding $\text{Cu}^{2+}/\text{Pb}^{2+}$ solutions. The HM content in the MOF sample after the sorption experiment was evaluated according to XRF analysis in (at.%) units (Table S3 in supplementary materials) and, for further clarity, converted to mmol per kg of MOF ($\text{mmol} \cdot \text{kg}^{-1}$).

According to the results, MIL-100 exhibited the highest Cu^{2+} ($2134.4 \text{ mmol} \cdot \text{kg}^{-1}$) and Pb^{2+} ($346.4 \text{ mmol} \cdot \text{kg}^{-1}$) ion sorption capacities. This correlation is believed to be associated with the available pore volume of this material. The high SSA and relatively large open pores provide ample sites for the adsorption of HM ions (Horcajada et al. 2007). Furthermore, in acidic media, negatively charged active sites are formed within the MIL-100 framework (Wu et al. 2023). This facilitates cation adsorption via electrostatic

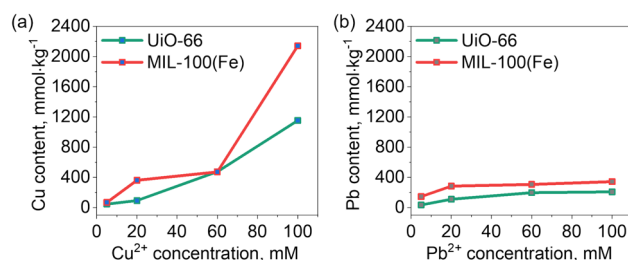
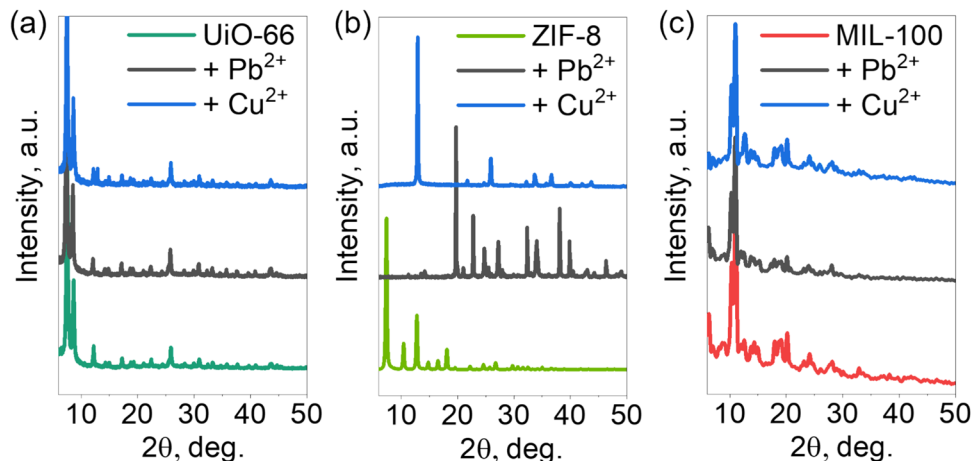


Fig. 3 The sorption capacity of UiO-66 and MIL-100 samples as a function of Cu^{2+} (a) and Pb^{2+} (b) solution concentrations

Fig. 2 XRD powder profiles of UiO-66 (a), ZIF-8 (b), and MIL-100 (c) samples before and after contact with 0.1 M solutions of $\text{Cu}(\text{NO}_3)_2$ (blue patterns) and $\text{Pb}(\text{NO}_3)_2$ (gray patterns)



interactions. In addition, surface complexation and ionic exchange with H^+ previously described mechanisms are proposed (Forghani et al. 2020). In this scenario, Cu^{2+} and Pb^{2+} could bind to the organic fragments of the MIL-100 crystals. Copper forms stronger bonds than Pb according to this mechanism, which could explain its higher sorption capacity (Joseph et al. 2021).

In summary, although the ZIF-8 sample possesses high SSA, its framework is unstable under acidic conditions induced by the hydrolysis of Cu^{2+} and Pb^{2+} salts. Both UiO-66 and MIL-100 demonstrated high stability. However, MIL-100 exhibited higher sorption capacity due to its higher porosity and specific active sites, which are capable of bonding with HM ions. Therefore, MIL-100 was selected to fabricate the nanocomposite.

Nanocomposite study

To create the nanocomposite, we used the WSB sample obtained under optimized synthesis conditions. Since MIL-100 was selected from the three MOFs under consideration, the WSB sample was incorporated during the MIL-100 synthesis, resulting in the formation of the WSB@MIL-100 composite. The XRD powder pattern of the WSB@MIL-100 sample shows characteristic peaks of MIL-100, confirming successful MIL-100 phase formation in the presence of WSB biochar (Fig. 4a).

Modifying the WSB surface with MIL-100 particles significantly increased the SSA. Figure 4b shows the N_2 adsorption/desorption isotherms of the WSB and the synthesized WSB@MIL-100 composite. The presence of the MOF fraction significantly affected the structure of the composite surface. First, the SSA of the WSB@MIL-100 nanocomposite was $419\text{ m}^2\cdot\text{g}^{-1}$, with a total pore volume of $0.194\text{ cm}^3\cdot\text{g}^{-1}$ (Fig. S8, Table S4 in supplementary materials). Therefore, coating the biochar with MIL-100 resulted in a sixfold increase in SSA. Secondly, the shape of the composite isotherm can be attributed to type I. This result was attributed microporous nature of MIL-100 and its extremely high SSA.

Its crystals covered the WSB particles, providing most of the active surface for the composite. Consequently, the composite acquired micropores from the MOF. However, unlike that of pure MIL-100, the isotherm of the composite contained an H4-type hysteresis loop. This suggests that the mesopore contributed to the composite by the WSB component.

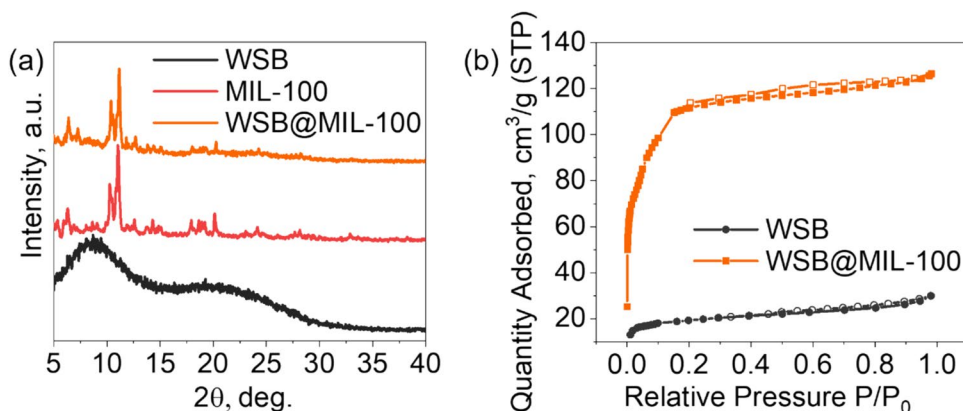
The increase in porosity of biochar-based composites after grafting MOFs is an expected outcome. For instance, the CBZ@UiO-66@ZnO/biochar composite reported by Ly et al. (2023) demonstrated SSA of $41\text{ m}^2\cdot\text{g}^{-1}$, while the ZIF-67/BC pyrolysis product achieved an SSA of $219\text{ m}^2\cdot\text{g}^{-1}$ (Zhang et al. 2023). Similarly, the BC/Mg-MOF-74 composite had an SSA of $146\text{ m}^2\cdot\text{g}^{-1}$ (Wang et al. 2024), and the composite based on MIL-53(Fe) and date palm stem biochar exhibited an SSA of approximately $96\text{ m}^2\cdot\text{g}^{-1}$ (Chakhtouna et al. 2023). A comparable SSA of $557\text{ m}^2\cdot\text{g}^{-1}$ was achieved by the ZIF-8 pyrolysis product applied to bamboo biochar (Zhang et al. 2024).

The WSB@MIL-100 composite demonstrated a notably high SSA of $419\text{ m}^2\cdot\text{g}^{-1}$. The value is significantly greater than the reported porosities of other similar composites, such as the waste rice straw biochar and MIL-100(Fe) composite ($133.9\text{ m}^2\cdot\text{g}^{-1}$) (Yuan et al. 2024) or the waste bamboo biochar and MIL-100(Al) composite ($44\text{ m}^2\cdot\text{g}^{-1}$) (Sun et al. 2025). These results highlight the exceptional performance of the WSB@MIL-100 composite developed in this research, underscoring its potential for advanced applications.

The WSB and WSB@MIL-100 samples were analyzed by scanning electron microscopy (SEM) analysis along with energy-dispersive X-ray spectroscopy (EDS) elemental mapping (Fig. 5).

Figure 5a shows the shape of the WSB particles, which retained the characteristic tissue structure of the original raw material. In Fig. 5c, elemental mapping reveals the absence of iron ions on the biochar surface, with only elements typical of such compounds present. The SEM images of the WSB@MIL-100 sample (Fig. 5b) reveal the formation of new particles on the WSB surface. EDS mapping was used

Fig. 4 a XRD patterns of the WSB, WSB@MIL-100, and MIL-100. b N_2 adsorption/desorption isotherms of WSB and WSB@MIL-100 samples. Filled markers represent the adsorption branches of the isotherms, while empty markers indicate the desorption branches



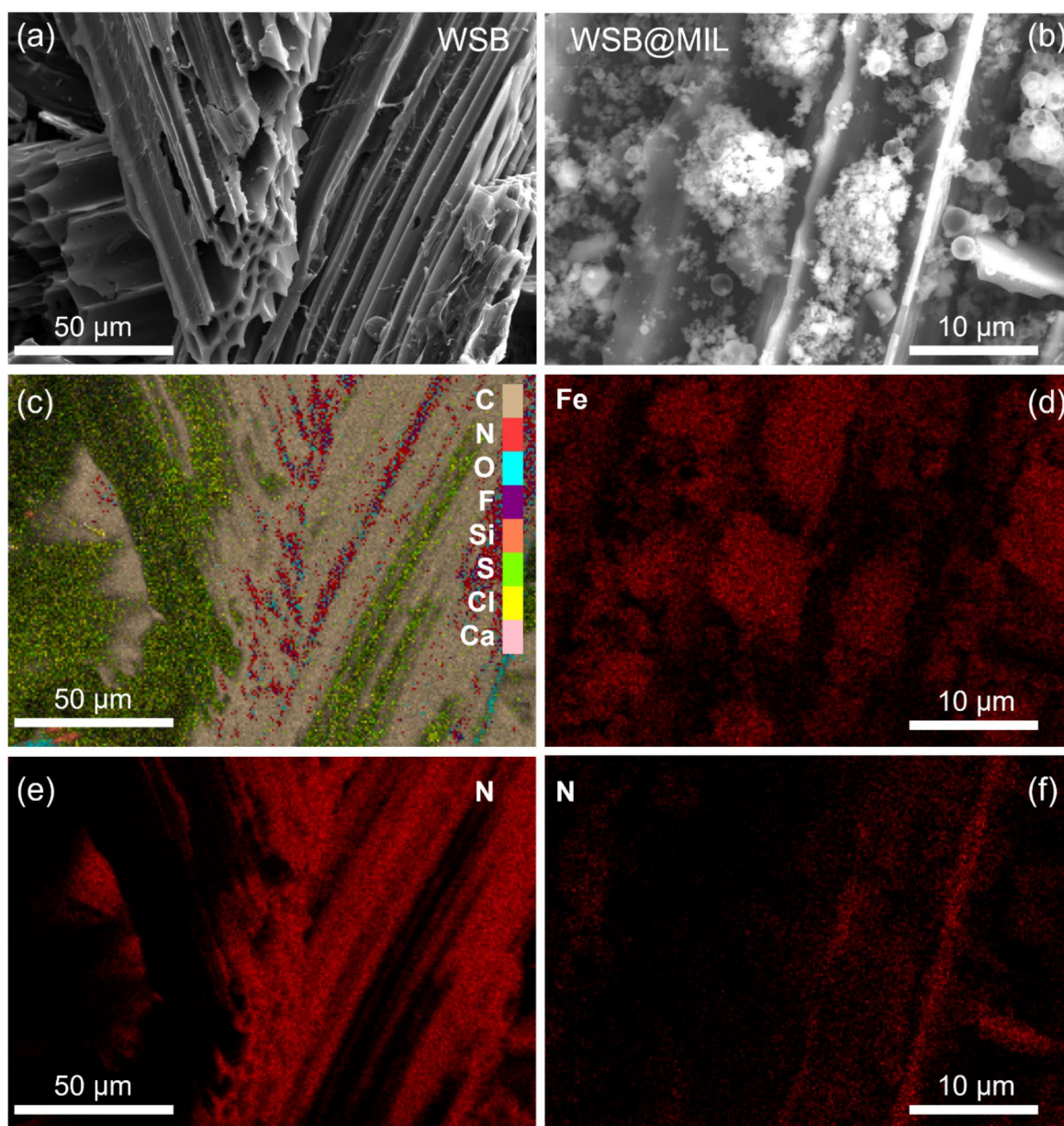


Fig. 5 SEM images of WSB (a) and WSB@MIL-100 nanocomposite (b). Part c shows EDS mapping the WSB sample, showing the distribution of C, N, O, F, Si, S, Cl, and Ca. Parts d–f represent selective

element distribution: Fe (d) and N (f) in WSB@MIL-100 and N (e) in WSB samples

to understand the composite's composition better. Most elements, such as carbon and oxygen, are common in both WSB and MIL-100. However, nitrogen was present only in the WSB biochar (Fig. 5e), whereas MIL-100 lacked this element. Conversely, iron ions were found only in the MIL-100 MOF, which the original biochar did not contain. Nitrogen and iron were thus used as indicators for distinguishing between the two phases—WSB and MIL-100. Figure 5e clearly shows Fe-containing particles on the biochar surface, while Fig. 5d highlights this surface by N-mapping.

Combined with powder XRD data, these results confirm the formation of uniformly distributed MIL-100 nanoparticles on the biochar surface.

In summary, the composite exhibits both micro- and mesopores, combining the surface properties of its individual components. The coexistence of mesopores and micropores in the WSB@MIL-100 composite enhances its sorption capacity. The micropores aid in the physical adsorption of HMs, whereas the mesopores facilitate the diffusion of pollutants, thus speeding up adsorption kinetics (Yang et al. 2019).

HM adsorption by nanocomposite

Characteristics of Cu²⁺ and Pb²⁺ adsorption on biochar and WSB@MIL-100-amended soil

The efficiency of the Cu²⁺ and Pb²⁺ adsorption from soil, both without and with sorbents, is shown in Fig. 6. The efficiency of HM removal from soil at the studied metal concentrations in solution (ranging from 0.5 to 10 mM) was shown to be for Cu 99–60% and for Pb 99–65%. It should be noted that the efficiency of HM removal decreased with increasing concentration of the initial solutions. The addition of biochar and nanocomposite to soil increased the HM removal efficiency. At low HM concentration (4 mM), both sorbents achieved high removal efficiency (> 98%). However, with the highest concentration (10 mM) of metal in solution, the efficiency decreased (to 82–89%, respectively) in the case of soil with biochar, which can be attributed to the occupation of free adsorption sites. In contrast, the soil with the WSB@MIL-100 nanocomposite exhibited a high removal efficiency (> 99%), even at high Cu²⁺ and Pb²⁺ concentrations in solution.

Figure 7 illustrates the results of sorption data fitting using the Langmuir and Freundlich models (Table S5 in supplementary materials). The Langmuir equation provided a better fit to the data than the Freundlich equation, with R^2 values ranging from 0.976 to 0.999. The superior fit of the experimental data to the Langmuir model suggests the homogeneous nature of the adsorbent surface, indicating that HM adsorption occurs at surface sites with similar binding energy levels (Cui et al. 2016).

The maximum adsorption (C_m) of HMs in soil increased after sorbent amendment, rising from 60.9–61.9 in untreated soil to 82.0–155.5 mmol·kg⁻¹ in sorbent-amended soils. This suggests that biochar and nanocomposite are more effective for metal sorption than bare soil. The Langmuir sorption affinity (K_L) value increased by 2.7–5.7 times for Cu²⁺ and 2.6–5.1 times for Pb²⁺, depending on the added materials (Table S5 in supplementary materials). In all cases, the highest C_m and K_L values were observed for Pb²⁺.

Fig. 6 Removal efficiency of Cu²⁺ (a) and Pb²⁺ (b) by untreated soil (green curves), soil with WSB sorbent (gray curves), and soil with WSB@MIL-100 nanocomposite (orange curves). Error bars represent \pm SD (standard deviation). Each experiment was conducted in triplicate ($n=3$)

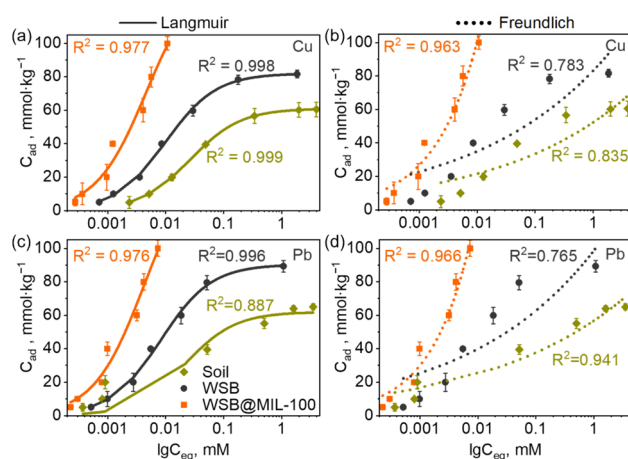
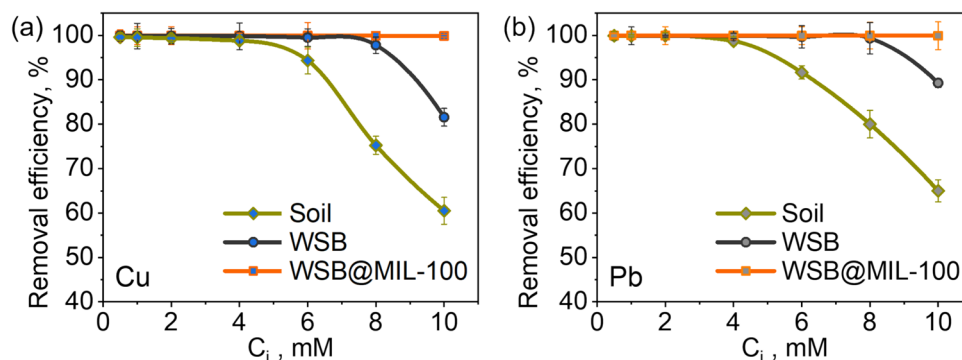


Fig. 7 Adsorption isotherms of Cu²⁺ (a, b) and Pb²⁺ (c, d) by untreated soil (green curves), soil with WSB sorbent (gray curves), and soil with WSB@MIL-100 nanocomposite (orange curves). Error bars represent \pm SD (standard deviation). Each experiment was conducted in triplicate ($n=3$). Solid lines indicate the Langmuir fitting of the sorption data, while dotted lines represent the Freundlich fitting. The graphs use logarithmic concentration axes for better visualization

With the addition of the WSB sample, the Freundlich adsorption affinity (K_F) of HMs increased by 1.6-fold for Cu²⁺ and 1.7-fold for Pb²⁺ compared with the original soil. The K_F value of soil amended with WSB@MIL-100 was 1443.1 L·kg⁻¹ for Pb²⁺ and 2220.1 L·kg⁻¹, which was much higher than that of soil with biochar, indicating promising application potential. This could be attributed to the larger SSA of WSB@MIL-100 (419 m²·g⁻¹) compared to WSB biochar (72 m²·g⁻¹), suggesting that the pore-filling effect was one of the main mechanisms of HM adsorption. The order of adsorbate positioning, determined by the C_m and K_F values, demonstrates the similarity between the Langmuir and Freundlich models (Table S5 in supplementary materials). However, across all cases, the K_F values exceeded the calculated C_m values, which is particularly notable in soils amended with the WSB@MIL-100 nanocomposite.

Thus, the nanocomposite with a high SSA and microporous structure displayed a strong affinity for HMs. Incorporating nanocomposite into the soil resulted in improved HM adsorption, thereby reducing the concentration of metals in the soil solution and their bioavailability.

Mechanisms of Cu^{2+} and Pb^{2+} adsorption

The XRD analysis results (Figure S10 in supplementary materials) of a non-contaminated soil sample indicated the presence of several mineral phases commonly found in the standard group, including quartz (SiO_2), enstatite (MgSiO_3), vaterite (CaCO_3), and titanomagnetite (Fe_2TiO_4). Additionally, the diffraction pattern of this sample shows contributions from an additional mineral phase, magnesium titanite (MgTi_2O_4). In the soil sample with the addition of WSB alongside the typical mineral phases found in the entire group (quartz, pyroxene, vaterite, and titanomagnetite), sylvite (KCl) was also identified (Fig. S11 in supplementary materials). The soil sample combined with the WSB@MIL-100 composite revealed the presence of quartz, pyroxene, calcite, and titanomagnetite. Notably, no contributions from other mineral phases were detected.

One of the mechanisms of the HM immobilization in soil may be the binding of HMs in the form of insoluble sediments. Literature analysis of studies of soils contaminated with Pb^{2+} suggests that soil samples may contain different mineral phases such as hydroxypyromorphite ($\text{Pb}_5(\text{PO}_4)_3(\text{OH})$), cerussite (PbCO_3), and hydrocerussite ($\text{Pb}_3(\text{CO}_3)_2(\text{OH})_2$). Other studies have confirmed the formation of pyromorphite-like minerals in lead-contaminated soils under the influence of phosphorus (Cao et al. 2002). In addition to those listed, anglesite (PbSO_4) and galena (PbS) are also common (Burt et al. 2003). Copper-contaminated soil typically contains mineral phases such as covellite (CuS) and other Cu-Fe sulfide-like minerals: moykhukite ($\text{Cu}_9\text{Fe}_9\text{S}_{16}$), talnakhite ($\text{Cu}_9(\text{Fe},\text{Ni})_8\text{S}_{16}$) (Mantha et al. 2019). There are also references to chalcocopyrite (CuFeS_2) (Křibek et al. 2010) and chalcocite (Cu_2S) (Ettler et al. 2014). However, XRD analysis of soil samples contaminated with Cu and Pb (Fig. S10 in supplementary materials) did not reveal new phases of HMs insoluble sediments. Weak differences in the intensity of the main peak do not allow us to talk about the appearance of additional mineral phases. In samples contaminated with Cu^{2+} and Pb^{2+} , only mineral soil phases such as quartz, pyroxene, and goethite ($\alpha\text{-FeO}(\text{OH})$) were detected. This could be for two reasons. Firstly, the large number of mineral phases in the soil, the low concentration of injected HMs ions, and the “noisiness” of the baseline may mask the presence of small amounts of HM-containing phases.

Secondly, this may be due to the predominance of ion exchange or complexation/sorption mechanisms. In this case, HM ions are strongly bound to sorbents or soil particles and cannot form their own mineral phases.

According to the EDX spectra, the addition of WSB and WSB@MIL-100 sorbents to the soil resulted in noticeable changes in the soil composition (Table S6). Specifically, the carbon concentration in the samples increased while the concentrations of other ions decreased. This is likely due to the fact that EDX detects only elements from the surface layer and can penetrate only a few micrometers into the sample. The porous WSB and WSB@MIL-100 materials adsorbed cations, reducing their surface concentration, while the biochar's carbon matrix increased the carbon content. A similar trend was observed when WSB and WSB@MIL-100 were added to soils contaminated with Cu^{2+} or Pb^{2+} , further supporting the occurrence of adsorption.

Figure 8 shows the distribution of Cu and Pb after adsorption by soil containing the WSB sample. It is evident that the HM ions are predominantly located on the surface of the sorbent, demonstrating effective decontamination by biochar adsorption.

Figure 9 displays soils with the WSB@MIL-100 composite after Cu/Pb exposure. Both ions were primarily found on the surface of the sorbents. A comparison of the distribution of Fe and the HMs reveals that higher concentrations of Cu and Pb coincide with Fe-rich regions, indicating adsorption by the MIL-100 MOF. However, the biochar support also contains HM traces.

To gain insights into the adsorption mechanisms, determine the composition and reveal the molecular structure of immobilized metals in soil with sorbents, in addition to traditional methods of adsorption estimation, such as X-ray absorption spectroscopy (Wang et al. 2022), chromatography (Ahmad et al. 2016), or inductively coupled plasma optical emission spectrometry (ICP-OES) (Lu et al. 2017); their combination with advanced X-ray spectral methods based on synchrotron radiation is more efficient (Liu et al. 2016). Synchrotron research techniques represent cutting-edge tools for providing detailed information on the bonding characteristics at the molecular level, the spatial environment of absorbed metals, and their interrelationship with neighboring elements, forming the local environment and coordination. In particular, Minkina et al. (2016) developed an approach to estimate the forms of interaction of Cu(II) and Zn(II) ions with soil components using fractionation techniques and XANES (extended X-ray absorption fine structure) spectroscopy. For the first time, data were obtained on the near-fine structure of X-ray spectra of HMs in Haplic Chernozem X-ray absorption near edge structure (XANES) that is widely used to

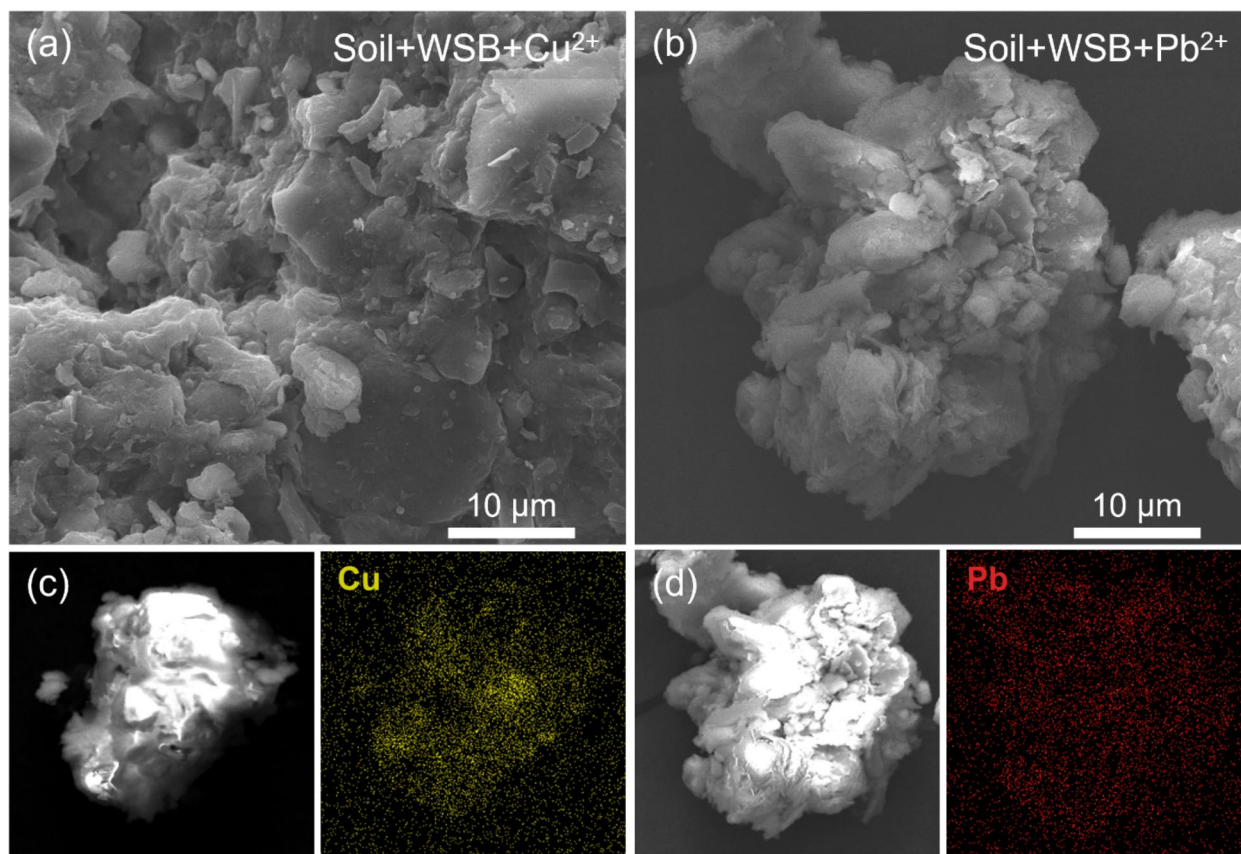


Fig. 8 SEM images of contaminated Haplic Chernozem with WSB admixture polluted with Cu^{2+} (a) and Pb^{2+} (b). Parts c and d show the area of the sample used for EDX mapping, with Cu (c) and Pb (d) distribution

study the electronic structure of matter. It helps determine the symmetry and energy of vacant molecular orbitals in molecules. The region of the far-edge fine structure of the X-ray absorption spectrum is characterized by the EXAFS method, which offers insights into the specific geometry surrounding the absorbing metal atom, detailing parameters such as coordination spheres and coordination numbers (Nevidomskaya et al. 2015). A weak absorption peak near the K-edge of the $\text{Cu}(\text{NO}_3)_2$ XANES spectra (Fig. 10a) was caused by the $1s \rightarrow 3d$ electron transition due to the bonding of Cu^{2+} in octahedral and tetrahedral positions.

The intensity of this peak depends on distortions that break the symmetry. The appearance of a shoulder in the absorption-edge region is linked to the $1s \rightarrow 4p$ dipole transition of the electron. The position of the EXAFS peaks (Fig. 10b) of a Cu-contaminated soil sample aligns with the proportional distances (without correction for phase shift) between the Cu^{2+} ion and atoms in local coordination shells, and the intense peak lies between 1.16 and 2.02 Å, due to

the O atoms of the first shell. Analysis of the spectra showed that the Cu^{2+} ions are encircled by four equatorial oxygen atoms and two axial oxygen atoms. The relatively short axial Cu–O distance suggests that ligands such as carboxylic acids or phenolic compounds replace equatorial molecules with Cu^{2+} . The main adsorption mechanism is the formation of surface copper complexes.

For the XAFS spectra of the Pb L_{III} edge (Fig. 10c, d) in the energy range 13,000–13,150 eV, the highest absorption intensity was observed at ~13,042 eV due to the $2p_{3/2} \rightarrow 6d$ transition. Thus, Pb^{2+} is involved in the formation of distorted complexes since adsorbed Pb ions can have different O–Pb–O bond angles (Jiang et al. 2023). The spectra of contaminated soil are characterized by a change in the parameters of the local environment, which indicates an increase in the length of the Pb–O bond and indicates the coordination of Pb in the form of a ligand. Note that the immobilization of Pb^{2+} during the introduction of biochar is carried out by organic carbon groups with the formation of cerussite PbCO_3 or hydrocerussite $\text{Pb}_3(\text{CO}_3)_2(\text{OH})_2$.

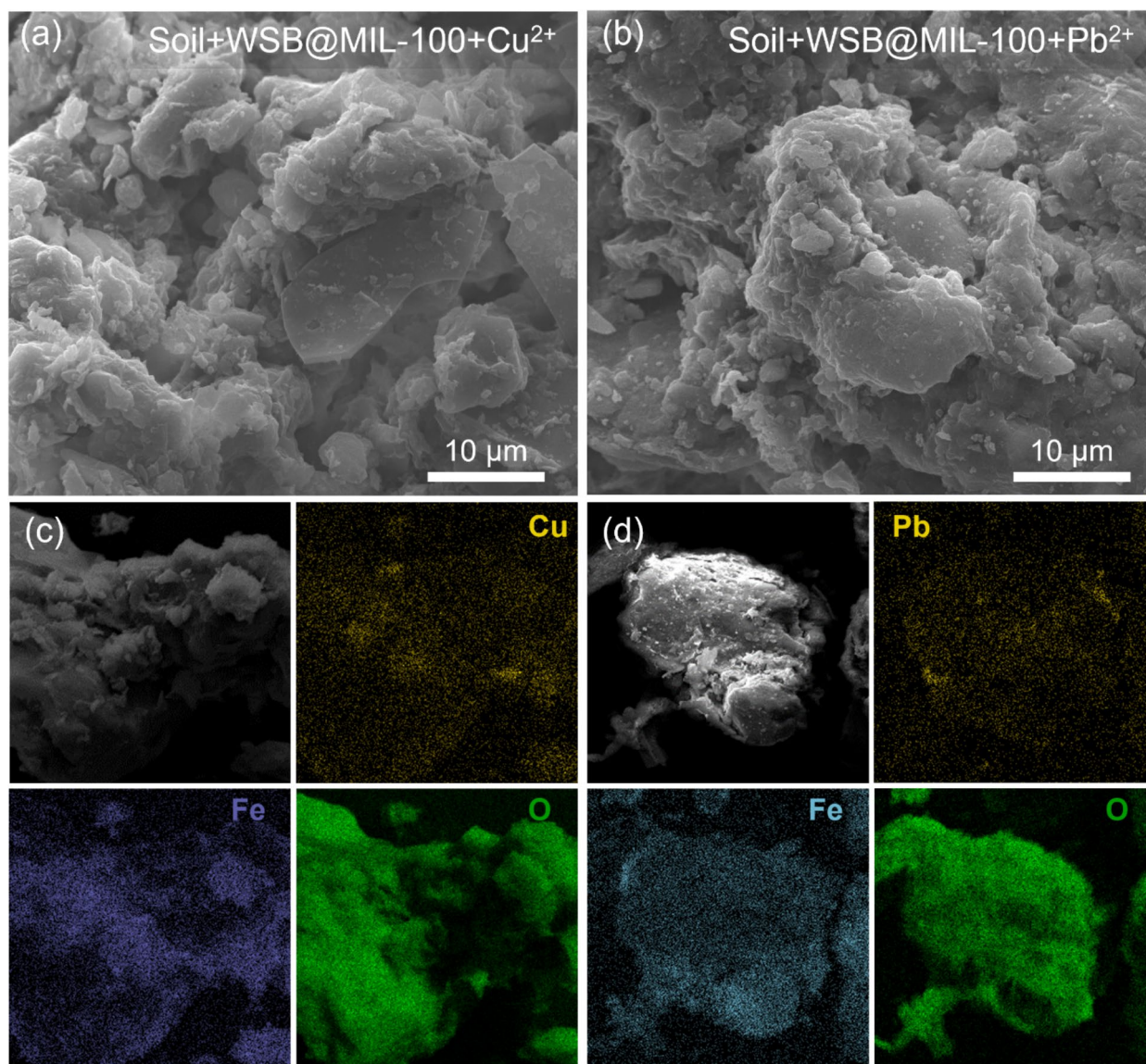


Fig. 9 SEM images of contaminated Haplic Chernozem with WSB@MIL-100 admixture polluted with Cu^{2+} (a) and Pb^{2+} (b). Parts c and d show the area of the sample used for EDX mapping, with Cu, Fe, and O (c) distribution and Pb, Fe, and O (d) distribution

XRD analysis revealed no new crystalline phases of Pb^{2+} or Cu^{2+} after adding WSB and WSB@MIL-100 to HM-contaminated soil. Element mapping showed that HM ions were distributed across both sorbents—the WSB biochar and the WSB@MIL-100 composite. To investigate the adsorption mechanism, element-sensitive techniques were employed. XANES and EXAFS spectra indicated that HM adsorption occurred primarily through bonding with functional groups on the surface of the WSB biochar. The biochar's dominance likely masked MIL-100's contribution; however,

EDX mapping revealed higher HM concentrations near Fe-rich regions, suggesting that MIL-100's active Fe centers also participated in adsorption. The quantitative changes in HM content with biochar and the nanocomposite reflect the complex nature of adsorption in multi-contaminant systems. A decrease in Na^+ , Mg^{2+} , K^+ , and Ca^{2+} cation content further indicated an ion-exchange process. Overall, the primary decontamination mechanisms were adsorption and ion exchange, with HM retention driven by biochar's functional groups and the Fe centers of MIL-100.

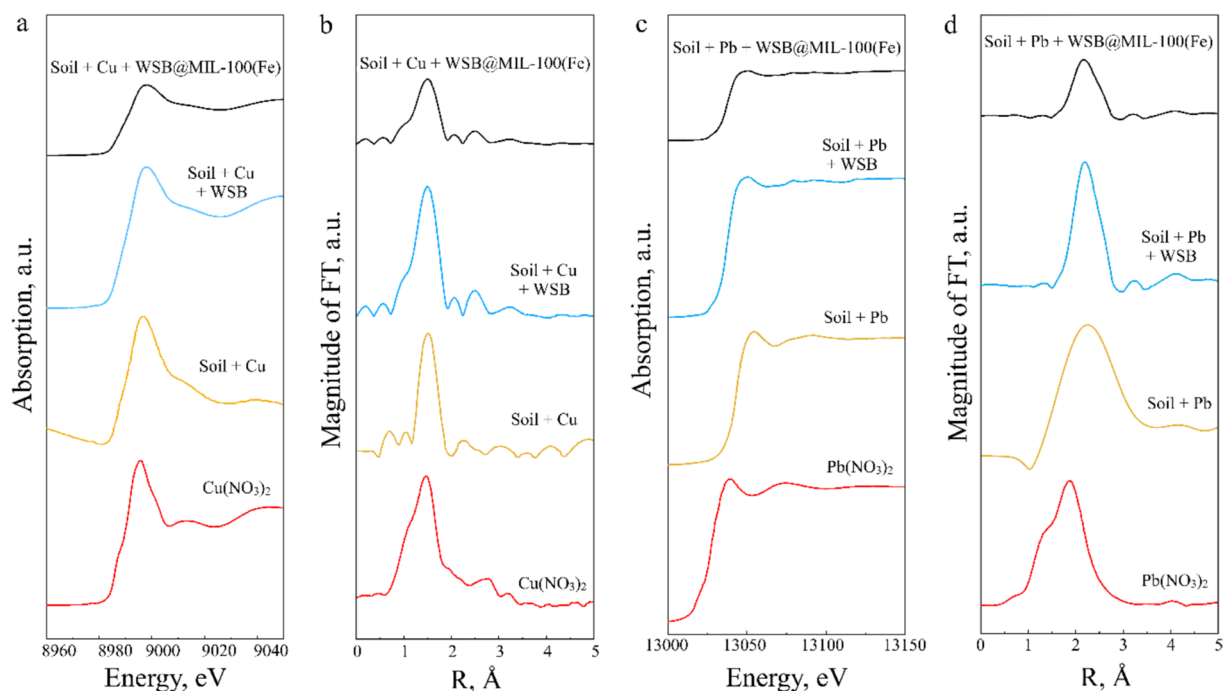


Fig. 10 XANES spectra of Cu K-edge (**a**) and Fourier transforms of EXAFS spectra (**b**) of contaminated Haplic Chernozem without and with the addition of biochar (WSB) and nanocomposite (WSB@MIL-100), as well as the reference $\text{Cu}(\text{NO}_3)_2$. Experimental XANES spec-

tra of the Pb L_{III} edge (**c**) and Fourier transforms (FT) of the EXAFS spectra (**d**) of contaminated Haplic Chernozem without and with the addition of biochar and nanocomposite, as well as the reference compound $\text{Pb}(\text{NO}_3)_2$

Conclusions

This study presents a novel technique for developing an effective composite for soil decontamination. The approach involved optimizing the synthesis conditions for wheat straw biochar (WSB), resulting in a material with enhanced porosity. To further improve its sorption capacity, the incorporation of MOFs into the composite was explored. Three MOFs—ZIF-8, UiO-66, and MIL-100—were evaluated for their performance. Although ZIF-8 exhibited high SSA, its framework was unstable in acidic conditions. Both UiO-66 and MIL-100 were stable during the adsorption of Pb^{2+} and Cu^{2+} , with MIL-100 demonstrating superior sorption capacity due to its higher porosity and active surface sites, which facilitated HM adsorption.

The nanocomposite was synthesized by incorporating WSB into the MIL-100 synthesis process. The

characterization techniques, including XRD, TEM, and EDX, confirmed the formation of the nanocomposite. The composite combined the microporosity of the MOF with the mesoporosity of biochar, showing sustained sorption efficiency even at high HM concentrations, which was not achievable with pure WSB.

When applied to contaminated soil, the nanocomposite significantly enhanced HM adsorption, reducing the concentration of metals in the soil solution and lowering their bioavailability. Mechanistic insights into HM adsorption were gained through a combination of XRD, SEM, EDX, and synchrotron EXAFS analyses, revealing two main interaction mechanisms: complexation and cation exchange. Overall, the nanocomposite demonstrated greater efficiency compared to pure biochar, highlighting its potential as an effective material for remediating soils contaminated with HM. Further research is needed to provide clear evidence of its long-term effects.

Supplementary Information The online version contains supplementary material available at <https://doi.org/10.1007/s11356-025-36052-9>.

Author contribution All authors contributed to the study conception and design. Material preparation and data collection were performed by Mikhail Kirichkov, Vera Butova, and Maksim Gritsai. Data analysis was performed by Tatiana Minkina and Alexander Soldatov. The first draft of the manuscript was written by Vladimir Polyakov, Tatiana Bauer, and Ekaterina Kravchenko, and all authors commented on previous versions of the manuscript. All authors read and approved the final manuscript.

Funding The study was supported by the Russian Science Foundation (project No. 22–76-10054) at the Southern Federal University. The authors express their gratitude to the ITMO University Core Facility Center “Nanotechnologies.”

Data availability The data used in this study are available from the corresponding author on reasonable request.

Declarations

Ethical approval No ethical approval was necessary for this study.

Consent to participate All participants in this study consent to participation.

Consent for publication All authors consent to this publication.

Competing interests The authors declare no competing interests.

References

- Abadin H, Ashizawa A, Stevens YW, Lladós F, Diamond G, Sage G, Quinones S, Bosch J, Swarts S (2007) Toxicological profile for lead. Agency for toxic substances and disease registry (US), Atlanta (GA)
- Abbas Q, Liu G, Yousaf B, Ali MU, Ullah H, Munir MAM, Liu R (2018) Contrasting effects of operating conditions and biomass particle size on bulk characteristics and surface chemistry of rice husk derived-biochars. *J Anal Appl Pyrol* 134:281–292. <https://doi.org/10.1016/j.jaap.2018.06.018>
- Ahmad M, Lee SS, Lee SE, Al-Wabel MI, Tsang DCW, Ok YS (2016) Biochar-induced changes in soil properties affected immobilization/mobilization of metals/metalloids in contaminated soils. *J Soils Sediments* 17(3):717–730. <https://doi.org/10.1007/s11368-015-1339-4>
- Ahmed HE, Rashed AE, El-Khouly ME, Albolqany MK, Abd El-Moneim A (2023) Green approach for sustainable production of paraffin fuel from CO₂ hydrogenation on Fe-MOF catalyst. *J Environ Chem Eng* 11(5):111071
- Anbalagan S, Jeevanantham S, Suresh K (2023) Biochar as sustainable strategy for remediation and regeneration of heavy metal-contaminated soil. In: pp 417–430. <https://doi.org/10.1515/9783110734003-020>
- Avcı C, Arinez-Soriano J, Carne-Sanchez A, Guillerm V, Carbonell C, Imaz I, Maspoch D (2015) Post-synthetic anisotropic wet-chemical etching of colloidal sodalite ZIF crystals. *Angew Chem Int Ed Engl* 54(48):14417–14421. <https://doi.org/10.1002/anie.201507588>
- Bordoloi N, Narzari R, Chutia RS, Bhaskar T, Katakı R (2015) Pyrolysis of *Mesua ferrea* and *Pongamia glabra* seed cover: characterization of bio-oil and its sub-fractions. *Bioresour Technol* 178:83–89. <https://doi.org/10.1016/j.biortech.2014.10.079>
- Brassard P, Godbout S, Lévesque V, Palacios JH, Raghavan V, Ahmed A, Hogue R, Jeanne T, Verma M (2019) Biochar for soil amendment. In: Char and carbon materials derived from biomass. pp 109–146. <https://doi.org/10.1016/B978-0-12-814893-8.00004-3>
- Bui VD, Tran TPA, Vu TH, Dao TP, Aminabhavi TM, Vasseghian Y, Joo S-W (2025) Integrating 3D-printed Mo₂CTx-UiO-66@rGQDs nanocatalysts with semiconducting BiVO₄ to improve interfacial charge transfer and photocatalytic degradation of atrazine. *Appl Catal b: Environ Energy* 365:124924. <https://doi.org/10.1016/j.apcatb.2024.124924>
- Burachevskaya M, Minkina T, Bauer T, Lobzenko I, Fedorenko A, Mazarji M, Rajput V (2023) Fabrication of biochar derived from different types of feedstocks as an efficient adsorbent for soil heavy metal removal. *Sci Rep* 13, 2020. <https://doi.org/10.1038/s41598-023-27638-9>
- Burt R, Wilson M, Keck T, Dougherty B, Strom D, Lindahl J (2003) Trace element speciation in selected smelter-contaminated soils in Anaconda and Deer Lodge Valley, Montana, USA. *Adv Environ Res* 8(1):51–67
- Butova, Budnik A, Bulanova E, Soldatov A (2016a) New microwave-assisted synthesis of ZIF-8. *Mendeleev Commun* 26(1):43–44. <https://doi.org/10.1016/j.mencom.2016.01.017>
- Butova, Soldatov MA, Guda AA, Lomachenko KA, Lamberti C (2016b) Metal-organic frameworks: structure, properties, methods of synthesis and characterization. *Russ Chem Rev* 85(3):280
- Butova, Budnyk AP, Bulanova EA, Lamberti C, Soldatov AV (2017) Hydrothermal synthesis of high surface area ZIF-8 with minimal use of TEA. *Solid State Sci* 69:13–21. <https://doi.org/10.1016/j.solidstatesciences.2017.05.002>
- Butova, Budnyk AP, Charykov KM, Vetlitsyna-Novikova KS, Bugaev AL, Guda AA, Lamberti C (2019) Partial and complete substitution of the 1,4-benzenedicarboxylate linker in UiO-66 with 1,4-naphthalenedicarboxylate: synthesis, characterization, and H(2)-adsorption properties. *Inorg Chem* 58(2):1607–1620. <https://doi.org/10.1021/acs.inorgchem.8b03087>
- Cao X, Ma LQ, Chen M, Singh SP, Harris WG (2002) Impacts of phosphate amendments on lead biogeochemistry at a contaminated site. *Environ Sci Technol* 36(24):5296–5304
- Cavka JH, Jakobsen S, Olsbye U, Guillou N, Lamberti C, Bordiga S, Lillerud KP (2008) A new zirconium inorganic building brick forming metal organic frameworks with exceptional stability. *J Am Chem Soc Commun* 130(42):13850–13851. <https://doi.org/10.1021/ja8057953>
- Chakhtouna H, Benzeid H, Zari N, Bouhfid R (2023) Microwave-assisted synthesis of MIL-53 (Fe)/biochar composite from date palm for ciprofloxacin and ofloxacin antibiotics removal. *Sep Purif Technol* 308:122850
- Chandra K, Proshad R, Islam M, Idris A (2023) An integrated overview of metals contamination, source-specific risks investigation in coal mining vicinity soils. *Environ Geochem Health* 45:7425–7458
- Chen D, Zhou J, Zhang Q (2014) Effects of heating rate on slow pyrolysis behavior, kinetic parameters and products properties of moso bamboo. *Biores Technol* 169:313–319. <https://doi.org/10.1016/j.biortech.2014.07.009>
- Cimò G, Kucerik J, Berns AE, Schaumann GE, Alonzo G, Conte P (2014) Effect of heating time and temperature on the chemical characteristics of biochar from poultry manure. *J Agric Food Chem* 62(8):1912–1918
- Cui X, Hao H, Zhang C, He Z, Yang X (2016) Capacity and mechanisms of ammonium and cadmium sorption on different wetland-plant derived biochars. *Sci Total Environ* 539:566–575. <https://doi.org/10.1016/j.scitotenv.2015.09.022>

- Ettler V, Konečný L, Kovářová L, Mihaljevič M, Šebek O, Křibek B, ... Vaněk A (2014) Surprisingly contrasting metal distribution and fractionation patterns in copper smelter-affected tropical soils in forested and grassland areas (Mufulira, Zambian Copperbelt). *Sci Total Environ* 473:117–124
- Forghani M, Azizi A, Livani MJ, Kafshgari LA (2020) Adsorption of lead(II) and chromium(VI) from aqueous environment onto metal-organic framework MIL-100(Fe): synthesis, kinetics, equilibrium and thermodynamics. *J Solid State Chem* 291:121636. <https://doi.org/10.1016/j.jssc.2020.121636>
- Fu T, Zhang B, Xing G, Cui S, Guan C-Y, Zhang Y, ... Peng Y (2022) Recent progresses, challenges, and opportunities of carbon-based materials applied in heavy metal polluted soil remediation. *Sci Total Environ* 856:158810. <https://doi.org/10.1016/j.scitotenv.2022.158810>
- Gholizadeh M, Hu X (2021) Removal of heavy metals from soil with biochar composite: a critical review of the mechanism. *J Environ Chem Eng* 9(5):105830. <https://doi.org/10.1016/j.jece.2021.105830>
- Gorban IE, Soldatov MA, Butova VV, Medvedev PV, Burachevskaya OA, Belanova A, ... Soldatov AV (2020) ^L-Leucine loading and release in MIL-100 nanoparticles. *Int J Mol Sci* 21(24):9758. <https://doi.org/10.3390/ijms21249758>
- Gouma V, Tziassiou C, Pournara A, Giokas D (2022) A novel approach to sorbent-based remediation of soil impacted by organic micro-pollutants and heavy metals using granular biochar amendment and magnetic separation. *J Environ Chem Eng* 10:107316. <https://doi.org/10.1016/j.jece.2022.107316>
- Horcajada P, Surble S, Serre C, Hong DY, Seo YK, Chang JS, ... Ferey G (2007) Synthesis and catalytic properties of MIL-100(Fe), an iron(III) carboxylate with large pores. *Chem Commun (Camb)* (27):2820–2822. <https://doi.org/10.1039/b704325b>
- Hou Y, Zhao Y, Lu J, Wei Q, Zang L, Zhao X (2023) Environmental contamination and health risk assessment of potentially toxic trace metal elements in soils near gold mines – a global meta-analysis. *Environ Pollut* 330:121803. <https://doi.org/10.1016/j.envpol.2023.121803>
- Jiang M, Wang K, Li G, Zhao Q, Wang W, Jiang J, ... Yuan L (2023) Stabilization of arsenic, antimony, and lead in contaminated soil with montmorillonite modified by ferrihydrite: efficiency and mechanism. *Chem Eng J* 457:141182
- Joseph L, Saha M, Kim S, Jun B-M, Heo J, Park CM, ... Yoon Y (2021) Removal of Cu²⁺, Cd²⁺, and Pb²⁺ from aqueous solution by fabricated MIL-100(Fe) and MIL-101(Cr): experimental and molecular modeling study. *J Environ Chem Eng* 9(6):106663. <https://doi.org/10.1016/j.jece.2021.106663>
- Kaur P, Sharma N, Kaur K (2023) Influence of pyrolysis temperature on rice straw biochar properties and corresponding effects on dynamic changes in bispyribac-sodium adsorption and leaching behavior in soil. *Pedosphere* 33(3):463–478. <https://doi.org/10.1016/j.pedsph.2022.06.046>
- Khan NA, Hasan Z, Jung SH (2013) Adsorptive removal of hazardous materials using metal-organic frameworks (MOFs): a review. *J Hazard Mater* 244–245:444–456. <https://doi.org/10.1016/j.jhazmat.2012.11.011>
- Khanmohammadi Z, Afyuni M, Mosaddeghi MR (2015) Effect of pyrolysis temperature on chemical and physical properties of sewage sludge biochar. *Waste Manag Res* 33(3):275–283. <https://doi.org/10.1177/0734242X14565210>
- Kravchenko E, Wang YC, Cruz TLD, Ng CWW (2023) Dynamics of carbon dioxide emission during cracking in peanut shell biochar-amended soil. *Sci Total Environ* 894:164922. <https://doi.org/10.1016/j.scitotenv.2023.164922>
- Kravchenko E, Minkina T, Mandzhieva S, Bauer T, Lacynnik E, Wong MH, Nazarenko O (2025) Ecological and health risk assessments of heavy metal contamination in soils surrounding a coal power plant. *J Hazard Mater* 484:136751
- Křibek B, Majer V, Veselovský F, Nyambe I (2010) Discrimination of lithogenic and anthropogenic sources of metals and sulphur in soils of the central-northern part of the Zambian Copperbelt Mining District: a topsoil vs. subsurface soil concept. *J Geochem Explor* 104(3):69–86. <https://doi.org/10.1016/j.jgexplo.2009.12.005>
- Leng L, Huang H, Li H, Li J, Zhou W (2019) Biochar stability assessment methods: a review. *Sci Total Environ* 647:210–222. <https://doi.org/10.1016/j.scitotenv.2018.07.402>
- Linnik VG, Bauer TV, Minkina TM, Mandzhieva SS, Mazarji M (2022) Spatial distribution of heavy metals in soils of the flood plain of the Seversky Donets River (Russia) based on geostatistical methods. *Environ Geochem Health* 44(2):319–333. <https://doi.org/10.1007/s10653-020-00688-y>
- Liu P, Ptacek CJ, Blowes DW, Landis RC (2016) Mechanisms of mercury removal by biochars produced from different feedstocks determined using X-ray absorption spectroscopy. *J Hazard Mater* 308:233–242. <https://doi.org/10.1016/j.jhazmat.2016.01.007>
- Lobzenko I, Burachevskaya M, Zamulina I, Barakhov A, Bauer T, Mandzhieva S, ... Rajput V (2022) Development of a unique technology for the pyrolysis of rice husk biochar for promising heavy metal remediation. *Agriculture* 12:1689. <https://doi.org/10.3390/agriculture12101689>
- Lu K, Yang X, Gielen G, Bolan N, Ok YS, Niazi NK, ... Wang H (2017) Effect of bamboo and rice straw biochars on the mobility and redistribution of heavy metals (Cd, Cu, Pb and Zn) in contaminated soil. *J Environ Manag*, 186(Pt 2):285–292. <https://doi.org/10.1016/j.jenvman.2016.05.068>
- Ly NH, Nguyen NB, Tran HN, Hoang TTH, Joo S-W, Vasseghian Y, ... Klemeš JJ (2023) Metal-organic framework nanopesticide carrier for accurate pesticide delivery and decrement of groundwater pollution. *J Clean Prod* 402:136809
- Madsen, Scarlett N, Kleeberg R, KK (2019) Reference intensity ratio methods. *International tables for crystallography (Vol. Volume H: Powder diffraction)*, vol H, ch 3.9, p 351
- Mantha H, Schindler M, Hochella MF (2019) Occurrence and formation of incidental metallic Cu and CuS nanoparticles in organic-rich contaminated surface soils in Timmins, Ontario. *Environ Sci: Nano* 6(1):163–179. <https://doi.org/10.1039/c8en00994e>
- Mazarji M, Bayero MT, Minkina T, Sushkova S, Mandzhieva S, Bauer TV, ... Wong MH (2023) Nanomaterials in biochar: review of their effectiveness in remediating heavy metal-contaminated soils. *Sci Total Environ* 880:163330
- Minkina TM, Soldatov AV, Nevidomskaya DG, Motuzova GV, Podkovyrina YS, Mandzhieva SS (2016) New approaches to studying heavy metals in soils by X-ray absorption spectroscopy (XANES) and extractive fractionation. *Geochem Int* 54(2):197–204. <https://doi.org/10.1134/s001670291512006x>
- Minkina TM, Linnik VG, Nevidomskaya DG, Bauer TV, Mandzhieva SS, Khoroshavin VY (2018) Forms of Cu (II), Zn (II), and Pb (II) compounds in technogenically transformed soils adjacent to the Karabashmed copper smelter. *J Soils Sediments* 18(6):2217–2228. <https://doi.org/10.1007/s11368-017-1708-2>
- Nevidomskaya DG, Minkina TM, Soldatov AV, Shuvaeva VA, Zubavichus YV, Podkovyrina YS (2015) Comprehensive study of Pb (II) speciation in soil by X-ray absorption spectroscopy (XANES and EXAFS) and sequential fractionation. *J Soils Sediments* 16(4):1183–1192. <https://doi.org/10.1007/s11368-015-1198-z>
- Nowacki W, Scheidegger R (1952) Die Kristallstrukturbestimmung des monoklinen, basischen Kupfernitrat Cu₄(NO₃)₂(OH)₆ II. *Helv Chim Acta* 35(1):375–390
- Nowotny H, Heger G (1986) Structure refinement of lead nitrate. *Acta Crystallogr C* 42(2):133–135

- Nunn B, Lord R, Minto J, Davidson CM, Manzoor N (2025) Surface soil-dust contamination of Phalaris arundinacea grown on former lead mine sites: Implications for biomass use, phytoremediation and phytomanagement. *Sci Total Environ* 958:178013. <https://doi.org/10.1016/j.scitotenv.2024.178013>
- Park KS, Ni Z, Côté AP, Choi JY, Huang R, Uribe-Romo FJ, ... Yaghi OM (2006) Exceptional chemical and thermal stability of zeolitic imidazolate frameworks. *Proc Natl Acad Sci* 103(27):10186–10191
- Peng Y, Huang H, Zhang Y, Kang C, Chen S, Song L, ... Zhong C (2018) A versatile MOF-based trap for heavy metal ion capture and dispersion. *Nat Commun* 9(1):187. <https://doi.org/10.1038/s41467-017-02600-2>
- Quan Y, Parker TF, Hua Y, Jeong H-K, Wang Q (2023) Process elucidation and hazard analysis of the metal–organic framework scale-up synthesis: a case study of ZIF-8. *Ind Eng Chem Res* 62(12):5035–5041
- Ragon F, Horcajada P, Chevreau H, Hwang YK, Lee U-H, Miller SR, ... Serre C (2014) In situ energy-dispersive X-ray diffraction for the synthesis optimization and scale-up of the porous zirconium terephthalate UiO-66. *Inorg Chem* 53(5):2491–2500
- Rajput V, Chernikova N, Minkina T, Gorovtsov A, Fedorenko A, Mandzhieva S, ... Wong M (2023) Biochar and metal-tolerant bacteria in alleviating ZnO nanoparticles toxicity in barley. *Environ Res* 220:115243. <https://doi.org/10.1016/j.envres.2023.115243>
- Rani L, Kaushal J, Srivastav AL, Mahajan P (2020) A critical review on recent developments in MOF adsorbents for the elimination of toxic heavy metals from aqueous solutions. *Environ Sci Pollut Res* 27(36):44771–44796. <https://doi.org/10.1007/s11356-020-10738-8>
- Rodrigues Cruz FJ, da Cruz Ferreira RL, Silva Conceição S, Lima EU, de Oliveira Neto CF, Rodrigues Galvão J, ... Viegas IdJM (2022) Copper toxicity in plants: nutritional, physiological, and biochemical aspects. In: Kimatu JN (Ed.), *Advances in Plant Defense Mechanisms*, pp 370. <https://doi.org/10.5772/intechopen.105212>
- Siidra O, Nekrasova D, Depmeier W, Chukanov N, Zaitsev A, Turner R (2018) Hydrocerussite-related minerals and materials: structural principles, chemical variations and infrared spectroscopy. *Acta Crystallogr Sect B: Struct Sci Cryst Eng Mater* 74(2):182–195
- Spokas KA (2010) Review of the stability of biochar in soils: predictability of O: C molar ratios. *Carbon Management* 1(2):289–303
- Sun W, Liu C, Liu S, Zhang J, Chen H, Qiu Z (2025) Effective adsorption of Congo red by an innovative biochar/LDH-derived MIL-100 (Al): investigation of coexisting pollutants and mechanism revelation. *Sep Purif Technol* 359:130670
- Thakur R, Sarvade S, Dwivedi B (2022) Heavy metals: soil contamination and its remediation. *Aatcc Rev* 10:59–76. <https://doi.org/10.58321/AATCCReview.2022.10.02.59>
- Tian M, Wang X, Liu F, Hu Q, Qiao Y, Wang Q (2023) Spatial-temporal variability and influence factors of Cd in soils of Guangxi, China. *PLoS ONE* 18:e0279980. <https://doi.org/10.1371/journal.pone.0279980>
- Tranchemontagne DJ, Mendoza-Cortés JL, O'keeffe M, Yaghi OM (2009) Secondary building units, nets and bonding in the chemistry of metal–organic frameworks. *Chem Soc Rev* 38(5):1257–1283
- Tu C, Wei J, Guan F, Liu Y, Sun Y, Luo Y (2020) Biochar and bacteria inoculated biochar enhanced Cd and Cu immobilization and enzymatic activity in a polluted soil. *Environ Int* 137:105576. <https://doi.org/10.1016/j.envint.2020.105576>
- Van Thang V, Tran Duy Nguyen N, Nadagouda MN, Aminabhavi TM, Vasseghian Y, Joo S-W (2024) Effective removal of perfluorooctanoic acid from water using PVA@UiO-66-NH₂/GO composite materials via adsorption. *J Environ Manag* 368:122248. <https://doi.org/10.1016/j.jenvman.2024.122248>
- Vasseghian Y, Nadagouda MM, Aminabhavi TM (2024) Biochar-enhanced bioremediation of eutrophic waters impacted by algal blooms. *J Environ Manag* 367:122044. <https://doi.org/10.1016/j.jenvman.2024.122044>
- Wang C, Jia L, Qin S, He L, Wu Y, Liu Q, Jin Y (2024) Study on the decarbonization mechanism of composite adsorbent by Mg-MOF-74-based modified biochar. *Fuel* 357:129959
- Wang, Kong X, Yang M, Xiong W, Li Z, Zhou H, ... Song Y-F (2022) Superstable mineralization of heavy metals using low-cost layered double hydroxide nanosheets: toward water remediation and soil fertility enhancement. *Ind Eng Chem Res* 62(1):365–374
- Wu J, Jin L, Wang N, Wei D, Pang M, Li D, ... Wang L (2023) Effects of combined application of chemical fertilizer and biochar on soil physio-biochemical properties and maize yield. *Agriculture* 13:1200. <https://doi.org/10.3390/agriculture13061200>
- Wuana R, Okieimen F (2011) Heavy metals in contaminated soils: a review of sources, chemistry, risks and best available strategies for remediation. *ISRN Ecol* 2011. <https://doi.org/10.5402/2011/402647>
- Yang X, Wan Y, Zheng Y, He F, Yu Z, Huang J, ... Gao B (2019) Surface functional groups of carbon-based adsorbents and their roles in the removal of heavy metals from aqueous solutions: a critical review. *Chem Eng J* 366:608–621. <https://doi.org/10.1016/j.cej.2019.02.119>
- Yuan Y, Wu G, Li W, Wang Y, Zhang TC, He G, Yuan S (2024) In situ growth of MIL-100 (Fe) onto the rice straw-derived biochar for efficient adsorption of gaseous ammonia. *Sep Purif Technol* 342:127034
- Zhang X, Zhang P, Yuan X, Li Y, Han L (2020) Effect of pyrolysis temperature and correlation analysis on the yield and physicochemical properties of crop residue biochar. *Biores Technol* 296:122318. <https://doi.org/10.1016/j.biortech.2019.122318>
- Zhang Z, Yu Q, Dai Y, Feng B (2023) Biochar supported magnetic ZIF-67 derivatives activated peroxy monosulfate for the degradation of ciprofloxacin: radical and nonradical pathways. *Colloids Surf A: Physicochem Eng Asp* 657:130559
- Zhang J, Rao G, Shao J, Zhang X, Zhang S, Zhang S, ... Chen H (2024) Porous nitrogen-doped biochar derived from ZIF-8-assisted pyrolysis of bamboo for efficient adsorption of SO₂. *Fuel* 367:131393
- Zhao B, O'Connor D, Zhang J, Peng T, Shen Z, Tsang DC, Hou D (2018) Effect of pyrolysis temperature, heating rate, and residence time on rapeseed stem derived biochar. *J Clean Prod* 174:977–987
- Zhou Y, Qin S, Verma S, Sar T, Sarsaiya S, Ravindran B, ... Awasthi MK (2021) Production and beneficial impact of biochar for environmental application: a comprehensive review. *Bioresour Technol* 337:125451. <https://doi.org/10.1016/j.biortech.2021.125451>

Publisher's Note Springer Nature remains neutral with regard to jurisdictional claims in published maps and institutional affiliations.

Springer Nature or its licensor (e.g. a society or other partner) holds exclusive rights to this article under a publishing agreement with the author(s) or other rightsholder(s); author self-archiving of the accepted manuscript version of this article is solely governed by the terms of such publishing agreement and applicable law.